

A Local Structural Basis to Resolve Amorphous Ices

Quinn M. Gallagher,^{1,*} Ryan J. Szukalo,^{2,*} Nicolas Giovambattista,^{3,4} Pablo G. Debenedetti,¹ and Michael A. Webb^{1,†}

¹*Department of Chemical and Biological Engineering,
Princeton University, Princeton, NJ 08544, United States*

²*Department of Chemistry, Princeton University, Princeton, NJ 08544, United States*

³*Department of Physics, Brooklyn College of the City University of New York, Brooklyn, New York 11210, United States*

⁴*Ph.D. Programs in Physics and Chemistry, The Graduate Center of
the City University of New York, New York, NY 10016, United States*

Phases with distinct thermodynamic properties must differ in their underlying distributions of microscopic structures. While ordered phases are readily distinguished by unit cells and space groups, the local structural basis differentiating amorphous phases is less apparent. Here, using a new probabilistic data-driven framework applied to molecular simulation data on water, we identify local collective variables that discriminate low-density and high-density amorphous (LDA and HDA) ices and characterize pressure-induced transitions between these phases. As expected, descriptors related to local density capably distinguish LDA and HDA; however, phase identity is surprisingly encoded within the first coordination shell. Furthermore, LDA transitions to HDA by a simple redistribution of LDA- and HDA-like environments with no evident intermediate structures, in accordance with a first-order-like transition that contrasts with the gradual evolution observed in other amorphous systems such as metallic glasses. These findings are robust across force fields, which themselves exhibit structural differences, and exemplify how other systems lacking obvious distinguishing features can be characterized.

I. INTRODUCTION

The thermodynamic properties that define macroscopic materials ultimately emerge from distributions of microscopic configurations.[1] In crystalline materials, the structural basis of a particular phase is encoded explicitly in unit cells and space groups, *i.e.*, macroscopic distinctions map cleanly onto symmetry-distinct local environments. For amorphous phases, by contrast, there is no obvious structural scaffold that plays an analogous role. If two amorphous phases are thermodynamically distinct, with different densities or response functions, then their underlying distributions of local environments must also differ.[2–4] What is far less clear is how they differ, over what length scales such differences are encoded, and whether they can be expressed in terms of a small number of collective variables that admit a microscopic interpretation.[5]

Water’s amorphous ices provide a particularly compelling arena to address the aforementioned questions. Low-density amorphous (LDA) and high-density amorphous (HDA) ice represent two glassy states with markedly different densities and thermodynamic behavior[6, 7], whose interconversion has long been discussed in the context of water’s putative liquid–liquid transition and associated polyamorphism [8–11]. LDA and HDA have been proposed as glassy analogs of the low-density and high-density liquid phases hypothesized to exist in supercooled water, making their structural distinction

relevant to long-standing questions about water’s anomalous behaviors. Clarifying the local structural basis that distinguishes LDA from HDA is thus central to connecting thermodynamic observations to the underlying statistical mechanics of water’s polyamorphic behavior [12, 13].

Prior studies have established that LDA exhibits a more open, tetrahedrally ordered network, whereas HDA is denser and more disordered [9, 14, 15]. This has been primarily deduced by examining physically motivated descriptors, including tetrahedral order parameters [16–18], bond-orientational order (BOO) metrics [19–21], coordination numbers, and local structure indices [17, 22, 23]. However, which specific descriptors most effectively encode this distinction and whether other key collective variables remain to be identified are open questions. A related question concerns spatial extent: how much local structural information is required to identify a phase? Recent studies of supercooled liquid water suggest that distinguishing low- and high-density environments requires correlations extending beyond the first coordination shell [20, 23]. Nevertheless, the extent to which this nonlocality arises from descriptor limitations rather than fundamental structural physics has not been systematically assessed.

A separate question concerns the microscopic character of the LDA–HDA transformation itself. Experimentally [6, 15, 24] and computationally[25–27], these glasses exhibit first-order-like transformations under pressure, yet the molecular-scale mechanisms remain unclear. Does the transformation proceed through structurally distinct intermediate environments, as observed in some metallic glasses, or does it involve redistribution between locally LDA-like and

* These authors contributed equally to this work.

† mawebb@princeton.edu

HDA-like motifs without intermediates [20, 28, 29]? The existence of very high-density amorphous ice (VHDA) as another distinct form [30, 31] demonstrates that water's amorphous landscape admits multiple structural states, making the possibility of intermediates along the LDA–HDA pathway a genuine question. For crystalline transitions, such questions are naturally addressed through symmetry breaking and defect structures; for amorphous phases, answering them requires direct, molecule-resolved access to the distribution of local environments and their evolution along transformation pathways, including the capacity to identify configurations that may belong to neither endpoint phase.

Existing analysis strategies struggle to address these questions simultaneously [32]. Simple low-dimensional order parameters are interpretable but can be biased by their construction, highlighting features that were anticipated and obscuring or unintentionally excluding important structural modes. High-dimensional descriptors [33, 34] can encode rich local information, and machine-learning classifiers built on these representations can achieve high discriminative accuracy [21, 35–40]. However, such models are often opaque. They classify without revealing which descriptors matter, and they lack calibrated uncertainties or mechanisms to detect out-of-distribution configurations. Consequently, while environments can be labeled as LDA or HDA, one cannot identify the minimal discriminative features, assess how local the distinction is, or determine whether transformation intermediates represent novel structures.

Here, we present a systematic investigation of the local structural basis distinguishing LDA and HDA and the microscopic character of their pressure-induced interconversion. This is facilitated by an interpretable probabilistic machine learning framework applied to molecular simulation data that addresses prior methodological deficiencies. This allows us to rank local structural descriptors by discriminative power through mutual-information analysis and construct a calibrated classifier capable of detecting out-of-distribution configurations. We find that interstitial hydrogen density dominates the discrimination and that phase identity is encoded within the first coordination shell. Analysis of transformation trajectories reveals no intermediate structures. Rather, the transition proceeds through redistribution of discrete LDA-like and HDA-like environments. These findings, robust across two water models derived from quantum chemistry, establish a well-defined and local structural basis that distinguishes LDA and HDA. More broadly, the approach provides a general recipe for identifying local collective variables in systems where distinct amorphous or disordered phases are known to exist but lack obvious distinguishing features.

II. METHODS

Figure 1 illustrates our framework that combines interpretable structural descriptors with probabilistic classification to identify local collective variables that distinguish amorphous phases. First, each molecule's local environment is represented using atom-centered symmetry functions (ACSFs) and bond-orientational order (BOO) parameters, which together provide a comprehensive, symmetry-invariant characterization of local structure (Step 1). Second, a two-stage feature selection procedure uses mutual information (MI) to rank descriptors by discriminative power and removes redundant descriptors through correlation analysis (Step 2). Third, class-conditional probability distributions of the selected descriptors are then modeled, enabling transparent probabilistic classification (Step 3). Finally, the joint probability for each class is used for molecule-by-molecule phase assignment and explicit detection of out-of-distribution configurations (Step 4). This approach automatically identifies which structural descriptors best distinguish phases without requiring *a priori* knowledge of the relevant order parameters, providing both high classification accuracy and physical interpretability. The following sections detail each step of this procedure.

A. Structural Descriptors

We consider two complementary, interpretable descriptor families that together provide a comprehensive characterization of microscopic environments. ACSFs encode the local environment through radially and angularly resolved correlations of interatomic distances [33]. BOO parameters [19] provide a complementary description that quantifies the orientational symmetry of the surrounding molecular arrangement and have been widely used to characterize amorphous and crystalline ices [20, 21]. Together, these descriptors form a symmetry-invariant and physically grounded representation of each molecule's local environment (Fig. 1, Step 1).

1. Atom-Centered Symmetry Functions

ACSFs are computed using several distinct functional forms that capture complementary aspects of local atomic environments through radially and angularly resolved correlations. All ACSF functions are centered on oxygen atoms (central oxygen atom i), with contributions included from both oxygen and hydrogen neighbors to ensure sensitivity to variations in hydrogen-bond motifs and proton arrangements not visible from oxygen positions alone. Throughout, we denote \mathbf{r}_{ij} as the displacement vector from central atom i to neighboring atom j and $R_{ij} = \|\mathbf{r}_{ij}\|$ as the corresponding scalar

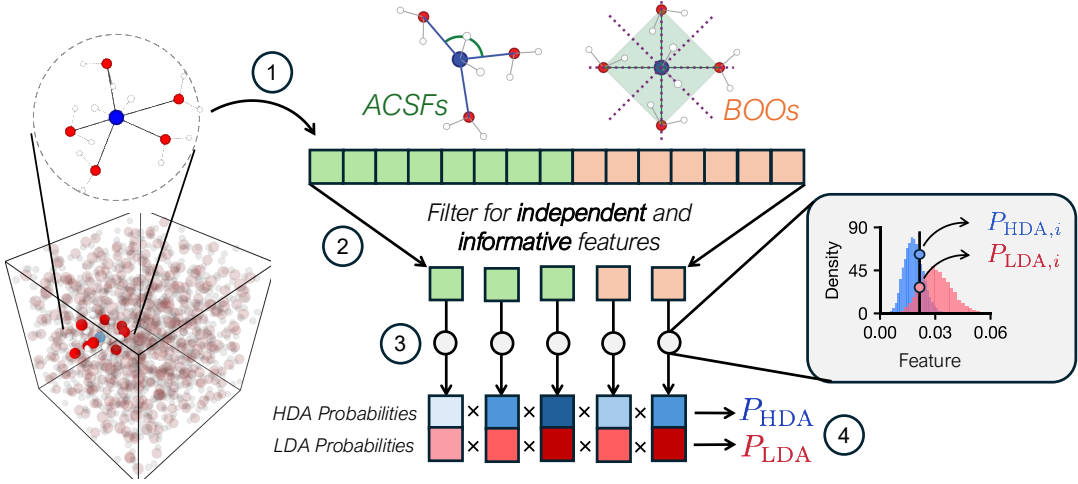


FIG. 1: Overview of the probabilistic classification framework. (1) Local atomic environments are sampled from MD simulations and represented using ACSF and BOO descriptors. (2) A two-stage feature-selection procedure removes redundant descriptors and identifies those most informative for distinguishing LDA and HDA. (3) For each selected descriptor and class, one-dimensional probability densities are estimated using Gaussian kernel density estimation. (4) The joint probability for each class is computed as the product of the descriptor-wise probabilities, providing an interpretable probabilistic classification and enabling explicit detection of out-of-distribution configurations.

distance. All ACSF functions employ a smooth cutoff function $f_c(R_{ij})$:

$$f_c(R_{ij}) = \begin{cases} 0.5 \left[\cos\left(\frac{\pi R_{ij}}{R_c}\right) + 1 \right] & \text{if } R_{ij} \leq R_c \\ 0 & \text{if } R_{ij} > R_c, \end{cases} \quad (1)$$

This cutoff function smoothly decays from 1 at $R_{ij} = 0$ to 0 at $R_{ij} = R_c$, with both the function and its first derivative vanishing continuously at the cutoff radius. We define the local environment around a central oxygen i by the 16 nearest neighboring water molecules. Let $\mathcal{N}_{\text{mol}}(i)$ denote this set of 16 neighbor molecules. We then define the corresponding sets of neighboring atoms as $\mathcal{N}_O(i)$ and $\mathcal{N}_H(i)$, the set of the 16 neighboring oxygen atoms and 32 neighboring hydrogen atoms belonging to the molecules in $\mathcal{N}_{\text{mol}}(i)$. Unless otherwise stated, we set $R_c \approx 5.0 \text{ \AA}$ and always ensure that all atoms in these neighbor sets satisfy $R_{ij} \leq R_c$ (*i.e.*, the neighbor list is defined by neighbor count).

Three types of radial symmetry functions provide complementary representations of the local density. The simplest radial function, G^1 , provides a weighted count of neighboring atoms:

$$G^1 = \sum_{j \in \mathcal{N}_\gamma(i)} f_c(R_{ij}), \quad (2)$$

where $\gamma \in \{\text{O}, \text{H}\}$ specifies the neighbor species set. In particular, we compute separate G^1 functions for oxygen and hydrogen neighbors, denoted G_O^1 and G_H^1 .

The next function, G^2 , focuses on the local density at a particular distance from the central atom,

$$G^2(\eta, R_s) = \sum_{j \in \mathcal{N}_\gamma(i)} \exp[-\eta(R_{ij} - R_s)^2] f_c(R_{ij}), \quad (3)$$

where η controls the width of the Gaussian and R_s shifts its center. By using multiple G^2 functions with different η and R_s values, these functions can construct a radially resolved representation of the local density.

The third function, G^3 , utilizes cosine damping:

$$G^3(\kappa) = \sum_{j \in \mathcal{N}_\gamma(i)} \cos(\kappa R_{ij}) f_c(R_{ij}), \quad (4)$$

where κ adjusts the period length. Using multiple G^3 functions with different κ values provides a Fourier-like decomposition of the radial distribution.

Two types of angular functions capture information about three-body configurations and local orientational order. This is achieved by considering angles centered at atom i formed by neighbor atoms j and k ,

$$\theta_{jik} = \arccos\left(\frac{\mathbf{r}_{ij} \cdot \mathbf{r}_{ik}}{R_{ij} R_{ik}}\right). \quad (5)$$

The two functions take the form (summing over unordered neighbor pairs $j < k$):

$$G^4(\eta, \zeta, \lambda) = 2^{1-\zeta} \sum_{j \in \mathcal{N}_\alpha(i)} \sum_{\substack{k \in \mathcal{N}_\beta(i) \\ k > j}} (1 + \lambda \cos \theta_{jik})^\zeta \times \exp[-\eta(R_{ij}^2 + R_{ik}^2 + R_{jk}^2)] f_c(R_{ij}) f_c(R_{ik}) f_c(R_{jk}), \quad (6)$$

and

$$G^5(\eta, \zeta, \lambda) = 2^{1-\zeta} \sum_{j \in \mathcal{N}_\alpha(i)} \sum_{\substack{k \in \mathcal{N}_\beta(i) \\ k > j}} (1 + \lambda \cos \theta_{jik})^\zeta \times \exp[-\eta(R_{ij}^2 + R_{ik}^2)] f_c(R_{ij}) f_c(R_{ik}). \quad (7)$$

Here, $\alpha, \beta \in \{\text{O, H}\}$ specify the neighbor species sets used for j and k . The parameter ζ controls the angular resolution, with larger values emphasizing specific angular arrangements, while $\lambda \in \{-1, 1\}$ shifts the sensitivity to linear ($\lambda = -1$) versus bent ($\lambda = 1$) configurations. The parameter η controls the radial extent over which angular correlations are evaluated. The key distinction between G^4 and G^5 lies in their radial dependencies. G^4 includes the neighbor–neighbor distance R_{jk} , restricting contributions to compact triplets where all three interatomic distances are small, while G^5 omits this constraint and thus captures angular correlations over a wider range of geometries. These angular functions are computed over all possible species combinations of the three atoms involved, with parameter sets chosen to capture angular correlations at different radial extents.

2. Bond-Orientational Order Parameters

BOO parameters provide a complementary description of local structure by quantifying orientational symmetry through spherical harmonics [19]. Unlike ACSFs which are explicitly constructed as sums over neighbors, BOO parameters characterize the angular distribution of the local environment in a rotationally invariant manner. For each oxygen atom i , we use the same oxygen neighbor list as above and define $N_b = |\mathcal{N}_\text{O}(i)| = 16$ neighboring oxygen atoms. The complex-valued order parameter q_{lm} is computed as:

$$q_{lm}(i) = \frac{1}{N_b} \sum_{j \in \mathcal{N}_\text{O}(i)} Y_{lm}(\theta_{ij}, \phi_{ij}), \quad (8)$$

where Y_{lm} are spherical harmonics of degree l and order m and (θ_{ij}, ϕ_{ij}) are the polar and azimuthal angles of the vector \mathbf{r}_{ij} connecting oxygen atoms i and j . The Steinhardt BOO parameter q_l is obtained by combining all m components for a given l :

$$q_l(i) = \sqrt{\frac{4\pi}{2l+1} \sum_{m=-l}^l |q_{lm}(i)|^2}. \quad (9)$$

Low values of l (e.g., $l = 3, 4$) are sensitive to tetrahedral and other low-symmetry arrangements, while higher l values capture more complex orientational motifs.

We also include third-order descriptors w_l , which provide additional sensitivity to the shape of the orientational distribution:

$$w_l(i) = \frac{\sum_{m_1+m_2+m_3=0} C_l^{m_1 m_2 m_3} q_{lm_1}(i) q_{lm_2}(i) q_{lm_3}(i)}{\left(\sum_{m=-l}^l |q_{lm}(i)|^2\right)^{3/2}}, \quad (10)$$

where $C_l^{m_1 m_2 m_3}$ are the Wigner 3- j coupling coefficients and the sum runs over all triplets (m_1, m_2, m_3) satisfying $m_1 + m_2 + m_3 = 0$. The w_l parameters are particularly useful for distinguishing structures with similar q_l values but different higher-order orientational correlations.

Additionally, We compute locally averaged variants that incorporate information from the neighborhood surrounding each molecule [41]. The locally averaged complex order parameter $\bar{q}_{lm}(i)$ is defined as:

$$\bar{q}_{lm}(i) = \frac{1}{N_b + 1} \left[q_{lm}(i) + \sum_{j \in \mathcal{N}_\text{O}(i)} q_{lm}(j) \right]. \quad (11)$$

This averaging procedure includes contributions from both the central molecule i and its N_b oxygen neighbors. From $\bar{q}_{lm}(i)$, we compute the rotationally invariant

$$\bar{q}_l(i) = \sqrt{\frac{4\pi}{2l+1} \sum_{m=-l}^l |\bar{q}_{lm}(i)|^2}. \quad (12)$$

The locally averaged descriptors \bar{q}_l provide enhanced discrimination between crystal structures compared to their unaveraged counterparts q_l , as the averaging reduces thermal fluctuations while preserving sensitivity to orientational order [41]. The corresponding locally averaged third-order descriptors \bar{w}_l are computed using (10) but with all $q_{lm}(i)$ substituted by $\bar{q}_{lm}(i)$.

Together with the ACSF descriptors, this comprehensive set of structural descriptors provides a detailed, physically interpretable representation of each oxygen-centered local environment.

B. Automatic Feature Selection

We extract the most informative descriptors from the full set using an automated ranking procedure (Figure 1, Step 2). We define local environments using the 16 nearest neighbors, consistent with prior work suggesting that distinguishing LDA from HDA requires incorporating the second solvation shell [20, 21, 23].

We assess the ability of each descriptor to discriminate between classes using mutual information (MI) [42]. MI quantifies the reduction in uncertainty about the class label upon observing a descriptor value and thus provides a model-free measure of discriminative power. For a feature X and class label Y , the MI is defined as:

$$\text{MI}(X; Y) = \sum_{x \in X} \sum_{y \in Y} p(x, y) \log \frac{p(x, y)}{p(x)p(y)}, \quad (13)$$

where $p(x, y)$ is the joint probability density of feature X and class label Y , and $p(x)$ and $p(y)$ are the corresponding distributions. We rank features by MI and retain those with MI values of at least 10% of the maximum observed MI, such that all features are expected to possess useful information.

To ensure that selected descriptors contribute distinct structural information, we use a greedy high-correlation filter. Proceeding in order of decreasing MI, each descriptor is retained only if its Pearson correlation with all previously retained descriptors satisfies $|r| < 0.8$. The outcome is a set of informative and roughly uncorrelated descriptors. Because the procedure operates on arbitrary descriptor inputs, it enables data-driven identification of discriminative descriptors without requiring prior assumptions about which structural motifs are important.

C. Probabilistic Model

The second component of our framework is a probabilistic classifier that assigns a label to each atomic environment as a calibrated likelihood of belonging to each structural class (Figure 1, Step 3). Rather than learning a decision boundary, we model the probability distribution of each selected descriptor for each class.

To avoid index ambiguity, we use $a \in \{1, \dots, m\}$ to index the selected m features and $n \in \{1, \dots, N_y\}$ to index training samples within class y . For each feature a and class y , we estimate the corresponding one-dimensional probability density $p_{a,y}(x)$ of observing value x using Gaussian kernel density estimation (KDE). Kernel bandwidths σ_a are selected via a grid search that maximizes the marginal log-likelihood estimated by five-fold cross-validation. Each KDE is normalized such that $\int_{-\infty}^{\infty} p_{a,y}(x) dx = 1$, where

$$p_{a,y}(x) = \frac{1}{N_y} \sum_{n=1}^{N_y} \frac{1}{\sqrt{2\pi\sigma_a^2}} \exp\left[\frac{-(x - x_{a,n})^2}{2\sigma_a^2}\right]. \quad (14)$$

Here, N_y is the number of samples for class y and $x_{a,n}$ are the observed values of feature a within that class.

Given an observed feature value x_a^* , we define the probability within a kernel window of half-width $0.5\sigma_a$ centered at x_a^* as

$$\pi_{a,y}(x_a^*) = \int_{x_a^* - 0.5\sigma_a}^{x_a^* + 0.5\sigma_a} p_{a,y}(x) dx. \quad (15)$$

For an environment characterized by m selected features, $\vec{x}^* = (x_1^*, x_2^*, \dots, x_m^*)$, we compute a class-conditional likelihood score under a naïve Bayes assumption (Figure 1, Step 4):

$$\mathcal{P}_y(\vec{x}^*) = \prod_{a=1}^m \pi_{a,y}(x_a^*). \quad (16)$$

Each environment is assigned the class with the largest likelihood score $\mathcal{P}_y(\vec{x}^*)$.

A further advantage of this probabilistic formulation is explicit out-of-distribution (OOD) detection. For each class y , we define a threshold $\mathcal{P}_{y,\text{cut}}$ as the 2nd percentile of $\mathcal{P}_y(\vec{x}^*)$ values on a held-out validation set. If a configuration satisfies $\mathcal{P}_y(\vec{x}^*) < \mathcal{P}_{y,\text{cut}}$ for all classes, it is labeled as OOD. This criterion ensures that the vast majority of in-distribution configurations are retained while enabling detection of novel or anomalous environments, a capability essential for analyzing structural transformations. This threshold can be adjusted to make the classifier more or less conservative, depending on the application requirements.

D. Training Data and Simulation Details

All configurations were obtained from the Deep Potential (DP) MD trajectories reported in Ref. 27. Two machine-learned potentials were employed, providing complementary representations of water’s potential energy surface. The first, DP_SCAN, was trained on electronic-structure data generated with the SCAN density functional [43, 44], a meta-GGA functional known to reproduce many of water’s structural and thermodynamic properties. The second, DP_MBpol, was trained on the many-body polarizable (MBpol) potential [45–48], which is parameterized against coupled-cluster reference data and is among the most accurate models of water available. All simulations were performed using LAMMPS (2 Aug 2023) [49] interfaced with DeePMD-kit (v3.0.0) [50, 51].

The training and evaluation dataset comprises of 10,000 molecular environments, equally divided between LDA and HDA. Configurations were selected from thermodynamic conditions where phase identity is unambiguous, avoiding the transition region to ensure reliable labels. LDA environments were drawn from isobaric quenches at temperatures at least 30 K below the glass transition and from isothermal compression at pressures at least 3 kbar below the transformation pressure. HDA environments were taken from compression trajectories at least 3 kbar above the transformation pressure and from decompression trajectories, the latter restricted to densities exceeding that of recovered HDA at 80 K and 1 bar to exclude partially transformed structures. As a benchmark for OOD detection, we curated 1,000 hexagonal ice (Ih) configurations. Ice Ih shares the tetrahedral hydrogen-bond network of LDA but exhibits long-range crystalline order absent in either amorphous phase, making it well-suited for evaluating OOD detection.

TABLE I: Comparison of model performance for LDA/HDA classification. Values represent the mean and standard deviation over five-fold cross-validation.

Model	HDA-Precision	HDA-Recall	LDA-Precision	LDA-Recall	Accuracy
BOO-NN	0.997 ± 0.001	0.997 ± 0.002	0.997 ± 0.002	0.997 ± 0.001	0.997 ± 0.001
PointNet	0.937 ± 0.008	0.988 ± 0.003	0.988 ± 0.003	0.934 ± 0.008	0.961 ± 0.003
AE-GMM	0.938 ± 0.008	0.982 ± 0.003	0.983 ± 0.003	0.935 ± 0.008	0.959 ± 0.003
Present Work (BOO)	0.997 ± 0.001	0.968 ± 0.010	0.967 ± 0.010	0.997 ± 0.001	0.982 ± 0.005
Present Work (ACSF)	0.973 ± 0.012	0.988 ± 0.009	0.987 ± 0.010	0.972 ± 0.013	0.980 ± 0.003
Present Work (BOO+ACSF)	0.996 ± 0.001	0.989 ± 0.003	0.989 ± 0.003	0.996 ± 0.001	0.993 ± 0.001

III. RESULTS AND DISCUSSION

A. Probabilistic classification effectively distinguishes HDA, LDA, and Ih

We begin by first assessing how accurately and confidently our framework can classify amorphous ice phases. To contextualize performance, we benchmark against three approaches with distinct strategies: a neural network trained on bond-orientational order parameters (BOO-NN) [20, 21], a coordinate-level architecture that learns representations directly from atomic positions (PointNet) [20, 21], and an autoencoder combined with Gaussian mixture modeling (AE-GMM) [39]. All models are trained using environments constructed from 16 nearest neighbors, following prior work [20, 21], and five-fold cross-validation is used to obtain robust estimates of precision, recall, and overall accuracy. Table I summarizes the results for DP_MBpol; analogous performance for DP_SCAN is provided in the SI (Table S1).

All approaches achieve accuracy exceeding 98%, confirming that LDA and HDA environments are distinguishable. BOO-NN achieves the highest accuracy (99.7%) [20, 21], while our method achieves 99.3%, surpassing both PointNet and AE-GMM and outperforming models trained on BOOs or ACSFs alone. This indicates that combining complementary descriptor types improves classification. Precision and recall are balanced across both phases for all methods, indicating no systematic bias. However, high classification accuracy alone does not guarantee reliability when analyzing transformations, where intermediate or novel environments may be encountered.

To assess detection of structures outside the known amorphous phases, we examine how models classify ice Ih environments, which share LDA’s tetrahedral coordination but exhibits long-range crystalline order. Figure 2 reveals pronounced differences among methods. BOO-NN and PointNet assign high LDA probabilities to many Ih configurations, yielding distributions that substantially overlap with genuine LDA environments. This overconfidence reflects a limitation of neural-network classifiers, which partition

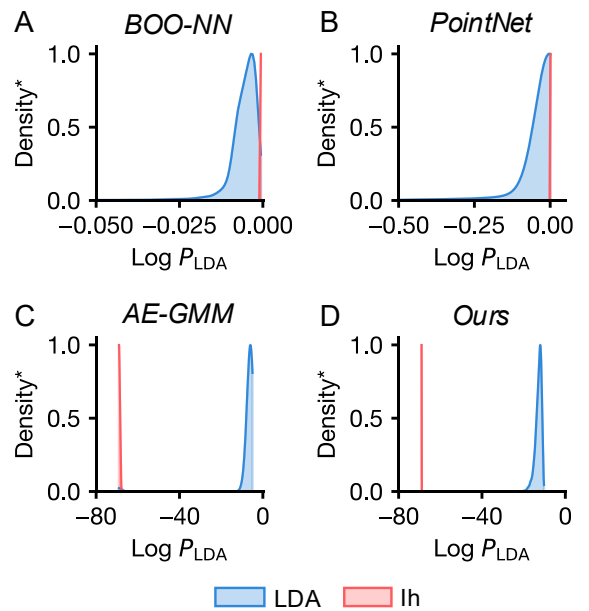


FIG. 2: Predicted LDA log-probabilities for true LDA environments (blue) and hexagonal ice Ih (red) for (A) BOO-NN, (B) PointNet, (C) AE-GMM, and (D) present work. ‘Density*’ refers to probability densities that are normalized so that their maximum value is 1.0.

descriptor space into fixed class regions without recognizing inputs outside the training distribution. In contrast, AE-GMM and our method assign Ih environments probabilities orders of magnitude lower than genuine LDA structures, producing well-separated distributions that enable reliable detection of novel configurations. This capability, arising from explicit modeling of class-conditional probability densities, is essential for analyzing transformation trajectories where intermediate or uncharacterized environments may exist.

B. Hierarchy of descriptor importance highlights key structural differences

To identify which structural descriptors most effectively distinguish LDA and HDA, we examine the descriptors selected by mutual-information analysis

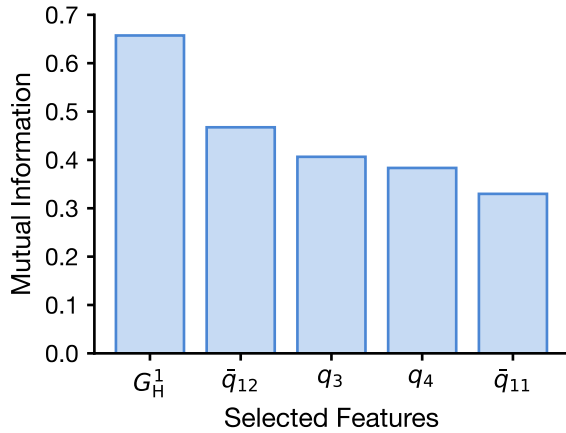


FIG. 3: Mutual information of descriptors selected for LDA/HDA classification. Features with higher mutual information are considered more useful for LDA/HDA classification.

in our probabilistic framework (Figure 3). Notably, the ACSF descriptor G_H^1 exhibits the highest MI, demonstrating that radial density information provides greater discriminatory power than the orientational symmetry captured by BOO parameters emphasized in prior work [20, 21]. The selected BOO parameters are consistent with those previously identified as changing significantly during LDA/HDA transitions [21]. These descriptors also work well for DP_SCAN configurations, indicating that they capture structural differences intrinsic to the phases rather than force-field-specific artifacts.

To understand the physical significance of these descriptors, we examine how they encode structural differences between phases. The most informative descriptor is G_H^1 , which can be interpreted as a weighted hydrogen count in the local environment of an oxygen, up to $R_c = 5.0 \text{ \AA}$ or ca. 16 water molecules (Figure 4A). HDA environments exhibit substantially larger G_H^1 values than LDA (Figure 4B), consistent with HDA's higher bulk density. Notably, local hydrogen density is more informative (higher MI) than the analogous oxygen-based descriptor G_O^1 ; this distinction emerges automatically from the descriptor selection. The remaining selected descriptors consist of BOO parameters, which, as defined in (9), quantify spherical symmetries of varying order across different length scales. Across all cases, LDA environments exhibit larger BOO values than HDA (Figures 4C–F). This behavior aligns with that of the conventional tetrahedral order parameter q , for which average values are $q \approx 0.91$ for LDA and $q \approx 0.74$ for HDA [27]. The HDA value is comparable to that of ambient liquid water, whose tetrahedrality is typically $q \approx 0.75$ [17], whereas LDA lies much closer to the highly ordered tetrahedral structure of ice Ih, which exhibits $q \approx 0.98$ [16, 17]. These results supply insight into the

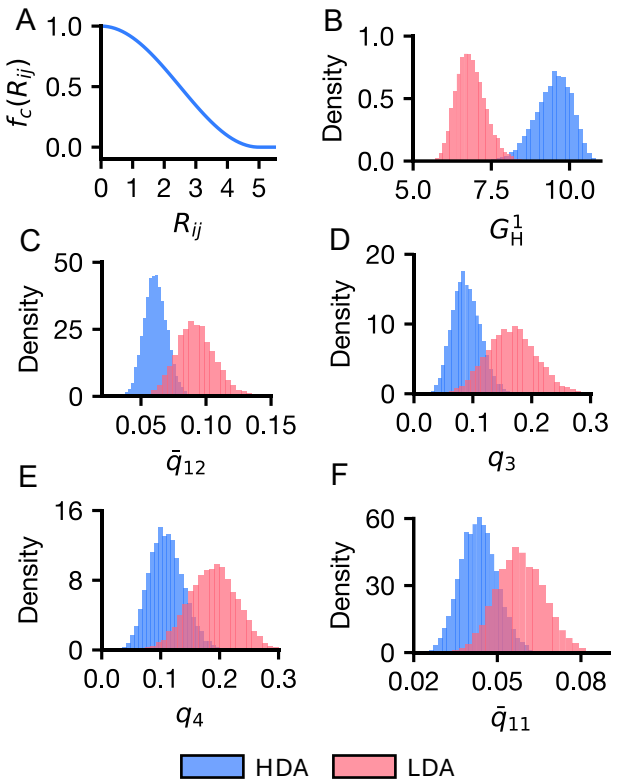


FIG. 4: Select order parameters distinguishing LDA and HDA environments. (A) The functional form of the $f_c(R_{ij})$ cutoff function used to compute the most informative descriptor. (B–F) The distribution of configurations from HDA (blue) and LDA (red) characterized by various local descriptors, ranked from most to the fifth-most informative. ‘Density’ refers to the normalized probability density for each descriptor.

relative importance of established structural signatures of water for discriminating its amorphous phases.

Taken together, these descriptors reveal that local environments are distinguished primarily through variations in local density, with orientational symmetry playing a secondary but complementary role. The prominence of density-based descriptors as the most informative descriptors is consistent with previous work identifying density as correlated with effective order parameters for liquid water near its critical point [22]. Within this low-dimensional descriptor space, individual molecular environments are classified as LDA or HDA based on their position along these axes, while environments falling outside the characteristic ranges of both phases are naturally identified as distinct.

C. LDA and HDA are resolvable within the first coordination shell due to interstitial hydrogen

A common feature of prior classification approaches for low- and high-density amorphous ice is the use structural

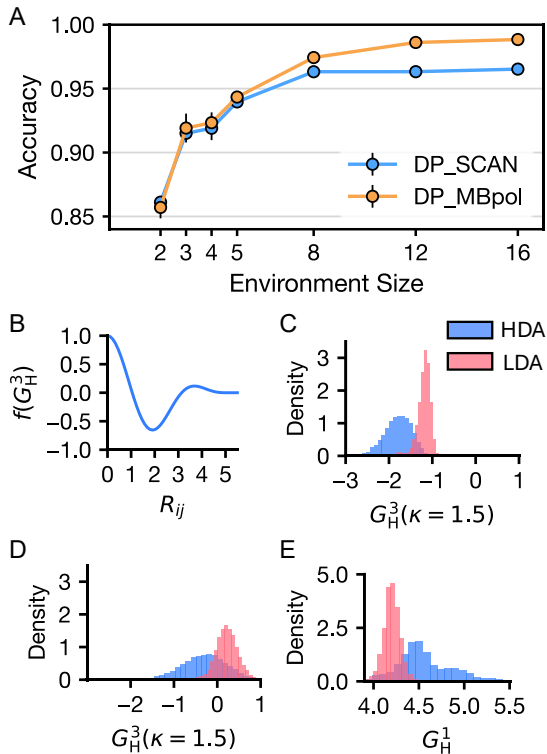


FIG. 5: Sensitivity of classification accuracy to environment size. (A) Classification accuracy as a function of atomic environment size, where size is the number of neighboring water molecules. Means and standard deviations are obtained from five-fold cross validation. (B) Function form of distance-dependent contributions to G_H^3 . Distributions from HDA and LDA environments characterized by (C) $G_H^3(\kappa = 1.5)$ using environments of size 3, (D) $G_H^3(\kappa = 1.5)$ using environments of size 16, and (E) G_H^1 using environments of size 3.

information that extend beyond the first coordination shell, incorporating 16 nearest neighbors [20, 21, 23]. This perspective is reinforced by studies of supercooled liquid water, where clear separation between low- and high-density environments emerges only when structural information is averaged beyond the first shell [23]. Motivated by these findings, we ask whether the same level of structural nonlocality is required to distinguish the glassy states. To this end, we compute ACSFs and BOO parameters for local environments containing between 2 and 16 nearest neighbors. By contrast to our prior analysis, we strictly retain only local (non-averaged) descriptors (*i.e.*, no \bar{q} or related quantities) to directly quantify the minimal information required for accurate classification.

Classification accuracy increases monotonically with environment size (Figure 5A), reaching approximately 86% with only two neighboring water molecules and plateauing above 95% for eight or more neighbors. These results indicate that the distinction between glassy LDA and HDA is encoded primarily in local

packing motifs and not nanometer-scale domains. That substantial phase-specific information is encoded within the immediate coordination shell is unexpected given prior work highlighting the necessity of second-shell information [20, 21, 23]. Rather, the modest improvement between eight and sixteen neighbors indicates that the LDA–HDA distinction is encoded primarily in local packing motifs within 5–7 Å, corresponding to a partial second solvation shell.

To understand what structural features most strongly delineate LDA and HDA at the smallest scales, we examine the most informative descriptors when considering only three neighboring water molecules. For both DP_SCAN and DP_MBpol, $G_H^3(\kappa = 1.5)$ is the most informative descriptor at this scale. The functional form (Figure 5B) takes negative values at distances between 1.5 and 3 Å, corresponding to hydrogen-bonded neighbors. HDA environments exhibit more negative values than LDA (Figure 5C), indicating higher hydrogen density within hydrogen-bonding distance of the central molecule. This aligns with the interpretation whereby densification causes the tetrahedral hydrogen-bond network of LDA to be disrupted by insertion of interstitial water molecules into the first coordination shell. The classifier effectively detects these interstitial hydrogens through G_H^3 , enabling accurate LDA–HDA discrimination, considering information within a solvation shell.

However, the informativeness of G_H^3 depends sensitively on spatial scale. This is demonstrated by computing its value using 16 neighboring water molecules and observing the substantial overlap between distributions LDA and HDA configurations (Figure 5D). Conversely, G_H^1 , the most informative descriptor for these larger environments, provides little separation at size 3 (Figure 5E). These contrasting behaviors indicate that different structural correlations dominate at different length scales. In particular, interstitial hydrogen insertion is most clearly distinctive at local scales, while the cumulative density differences captured by G_H^1 emerge only when averaging over larger environments.

The success of purely local descriptors in distinguishing glassy LDA and HDA may appear to contrast with observations in supercooled liquid water, where clear separation between low- and high-density environments requires length scales approaching 1 nm [23]. These findings are complementary rather than contradictory. Near criticality, density fluctuations are collective and spatially extended, necessitating nonlocal descriptors. In the vitrified glasses studied here, these same local motifs are arrested into distinct basins of configuration space, rendering differences in interstitial occupancy and tetrahedral order sufficiently pronounced that first-shell information alone yields accurate classification.

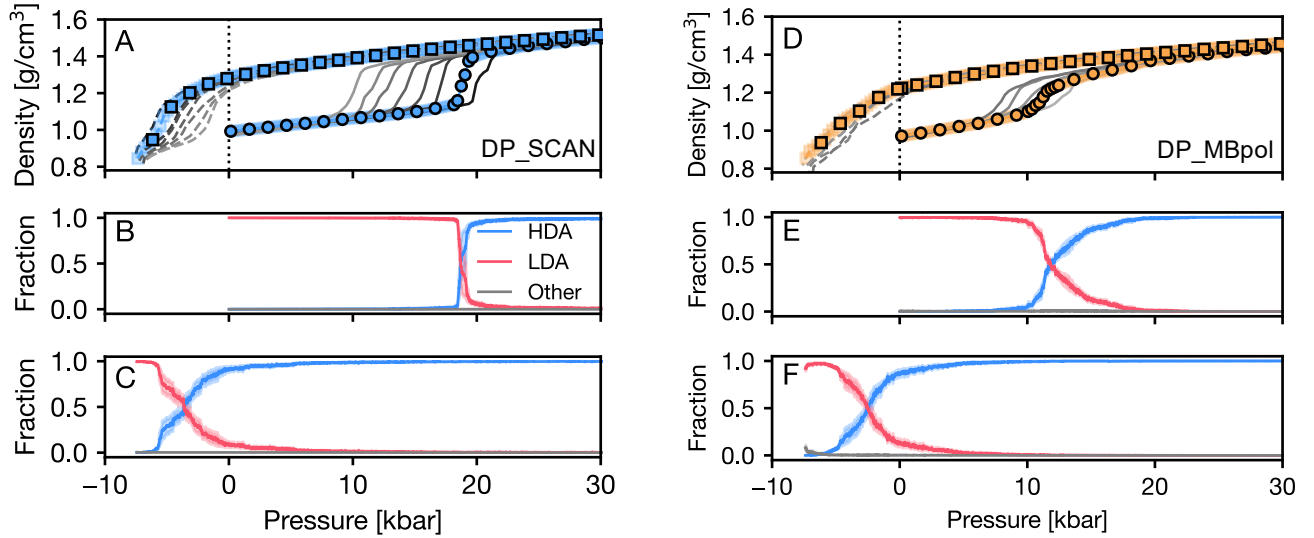


FIG. 6: Analysis of compression and decompression trajectories at $T = 80$ K. (A) Density–pressure equation of state (EOS) for DP_SCAN across all temperatures ranging from 60–200 K. The $T = 80$ K curve is highlighted in blue with circles (compression) and squares (decompression), while the gray curves show data for other temperatures.[27] (B,C) LDA, HDA, and outlier fractions for DP_SCAN compression and decompression at 80 K. (D) EOS for DP_MBpol, plotted analogously to (A). (E,F) LDA, HDA, and outlier fractions for DP_MBpol compression and decompression at 80 K. All composition curves are averaged over three independent trajectories and the shaded regions denote one standard deviation.

D. Redistribution of local environments underlies transition and highlights first-order character

We next consider the microscopic character of the LDA–HDA transformation. Specifically, does it proceed through structurally distinct intermediate environments or via redistribution between locally LDA-like and HDA-like motifs? Experimentally, these phases can be interconverted via isothermal compression and decompression, with signatures commonly interpreted as first-order-like transitions [6, 15, 24]. We therefore apply our classifier to isothermal compression and decompression trajectories at $T = 80$ K for both water models [27], labeling each molecule at every timestep as LDA, HDA, or outlier based on its local environment. Figure 6 summarizes the transformation behavior.

Both models exhibit first-order-like signatures, though with distinct characteristics. For DP_SCAN, compression produces a sharp transformation near 18 kbar. The LDA fraction collapses abruptly while the HDA fraction rises nearly discontinuously (Figure 6A,B). Decompression proceeds more gradually at slightly negative pressures, with LDA and HDA environments coexisting over an extended pressure range (Figure 6C), indicating pronounced hysteresis. DP_MBpol displays smoother behavior, in that the LDA→HDA transition unfolds continuously over approximately 8–16 kbar during compression (Figure 6D,E). Decompression again requires slightly negative pressures (Figure 6F). Despite these kinetic differences, the transformation in both models strikingly proceeds entirely through changes

in the relative populations of LDA- and HDA-like environments, with no intermediate motifs observed.

The absence of intermediates carries important mechanistic implications. The $\text{LDA} \leftrightarrow \text{HDA}$ transformation can be understood as a redistribution of local environments between two distinct structural basins, without an intervening metastable state. This population-based picture is consistent with long-standing views that LDA and HDA correspond to separate minima on the underlying potential energy landscape [12, 13], and provides direct molecular-scale evidence for the first-order-like character of the transition.

E. Local structural motifs reliably map LDA/HDA phase boundaries

Analysis of compression and decompression trajectories over a range of temperatures allows for approximate identification of the LDA/HDA spinodals by mapping the limits of mechanical stability. Conventionally, transition pressures are estimated from the rate-dependent density–pressure equation of state (EoS), where the LDA→HDA transformation appears as a maximum in the rate of density change. However, the reverse HDA→LDA transition seemingly lacks clear thermodynamic signatures, particularly for DP_MBpol, where no reliable decompression spinodal could be previously obtained [27]. To overcome this limitation, we use molecule-resolved phase classification as a structural criterion, defining the transition pressure

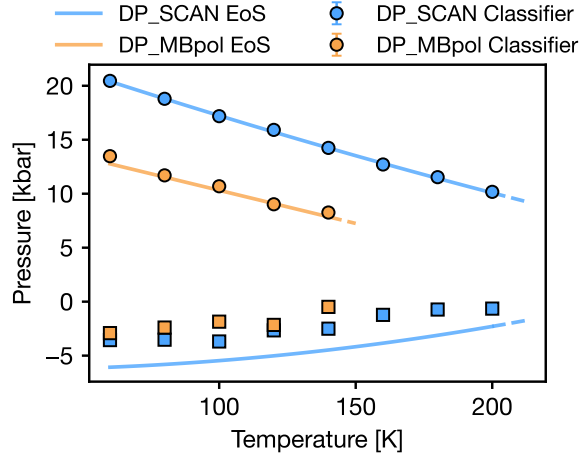


FIG. 7: Transition pressures for the DP_SCAN and DP_MBpol water models using density-pressure equation of state (EoS) [27] and classifier-derived 50/50 composition criteria (Classifier). Circles denote compressions and squares denote decompressions. The DP_MBpol EoS is not present for decompressions because no reliable decompression spinodal could be identified.

as the point of equal LDA and HDA populations.

For compression trajectories, classifier-derived and EoS-based transition pressures agree quantitatively for both models (Figure 7, circles), reflecting strong coupling between local structural reorganization and macroscopic densification. For decompression, the classifier robustly identifies HDA \rightarrow LDA transition pressures even where the EoS varies continuously without inflection (Figure 7, squares). This enables construction of complete kinetic phase diagrams, including the decompression spinodal for DP_MBpol that was previously inaccessible from thermodynamic analysis alone. Furthermore, both water models exhibit substantial hysteresis, with decompression transitions occurring at negative pressures and differing from compression pressures by 15–25 kbar. This behavior is consistent with large kinetic barriers characteristic of first-order-like transformations.

F. Structural pathways of pressure-induced transformations exhibit hysteresis

The substantial hysteresis in transition pressures and the capacity to resolve them with local descriptors raises questions: do compression and decompression follow identical structural pathways, or does the transformation mechanism differ between forward and reverse directions? To gain insight into the mechanistic progression of the phase transformation, we track the average descriptor values along the (de)compression trajectories. Figure 8 presents the results, characterizing local environments with three complementary descriptors across temperatures ranging from 60 to 140 K, for

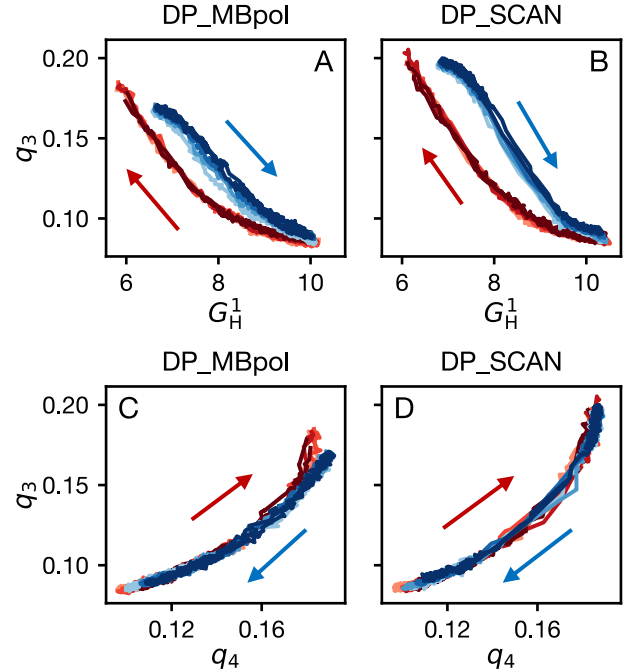


FIG. 8: Evolution of local environment descriptors during compression (blue) and decompression (red) from 60 K to 140 K. (A,B) Trajectories in q_3 – G_H^1 space for DP_MBpol and DP_SCAN reveal distinct forward and reverse pathways. (C,D) Trajectories in q_3 – q_4 space show apparent reversibility. Arrows indicate direction of progression; lighter shades correspond to lower temperatures.

DP_MBpol and DP_SCAN.

Both water models exhibit pronounced microscopic hysteresis when considering evolution of the BOO parameter q_3 alongside the local hydrogen density descriptor G_H^1 (Figure 8A,B). Compression (blue) and decompression (red) trajectories follow clearly distinct paths, revealing different mechanisms for the forward and reverse transformations. Compression proceeds through three distinct structural stages. In the initial stage, structures densify with minimal loss of orientational order, corresponding to an increase in G_H^1 at nearly constant q_3 . This regime reflects elastic compression of the LDA hydrogen-bond network without substantial topological rearrangement. In the second stage, tetrahedral order collapses while densification continues, marking the breakdown of the low-density network structure. The final stage involves further densification within the HDA basin, with little additional change in orientational order. Temperature primarily affects the second stage. Specifically, higher temperatures allow the collapse of tetrahedral order to occur at slightly higher hydrogen coordination.

Decompression trajectories show a qualitatively different sequence. Density decreases substantially before any significant recovery of tetrahedral order;

TABLE II: Features selected by our model and their mutual information for DP_SCAN/DP_MBpol classification. Here, we consider features chosen to classify LDA environments generated by either DP_SCAN or DP_MBpol.

Feature	Mutual Information
$G_O^2(\eta = 2.5, R_s = 1.0)$	0.220
$G_H^2(\eta = 1.0, R_s = 1.0)$	0.188
$G_{H,H}^5(\eta = 4.5, \zeta = 0.5, \lambda = -1.0)$	0.142
$G_H^3(\kappa = 0.5)$	0.141
$G_O^3(\kappa = 2.0)$	0.117

q_3 increases only after the system has expanded well into the low-density regime. These distinct forward and reverse pathways demonstrate that the LDA \rightarrow HDA and HDA \rightarrow LDA transformations proceed via different microscopic mechanisms when viewed through descriptors encoding both local density and orientational symmetry.

The apparent reversibility depends on descriptor choice. When the local hydrogen density (*i.e.*, G_H^1) is replaced by the BOO parameter, q_4 , compression and decompression trajectories collapse onto nearly identical curves for both water models (Figure 8C,D). From this perspective, the transformation appears effectively reversible, with the system retracing the same structural pathway in both directions. SI Figs S2 and S3 show that any combination of the four optimal BOO parameters yields apparently reversible transitions, whereas including the ACSF-based G_H^1 reveals pronounced microscopic hysteresis.

This contrast underscores that the microscopic interpretation of amorphous phase transformations depends sensitively on which structural features are examined. If analysis were restricted to BOO parameters alone, one might incorrectly infer that the LDA \leftrightarrow HDA interconversion is governed by a single, symmetric reaction coordinate dominated by oxygen packing. Instead, we find pronounced hysteresis in the evolution of local environments—consistent across temperatures and force fields—that would remain completely obscured using only conventional structural metrics.

G. Different force fields produce locally distinct LDA phases

The preceding analysis highlights qualitative similarities but also systematic differences with respect to transformation kinetics and pathways between DP_SCAN and DP_MBpol. An intriguing and fundamental question is whether these force fields produce structurally distinguishable local environments even within the same amorphous phase. To address this, we now utilize the data-driven framework to test whether local environments generated by DP_SCAN can be distinguished from DP_MBpol, rather than

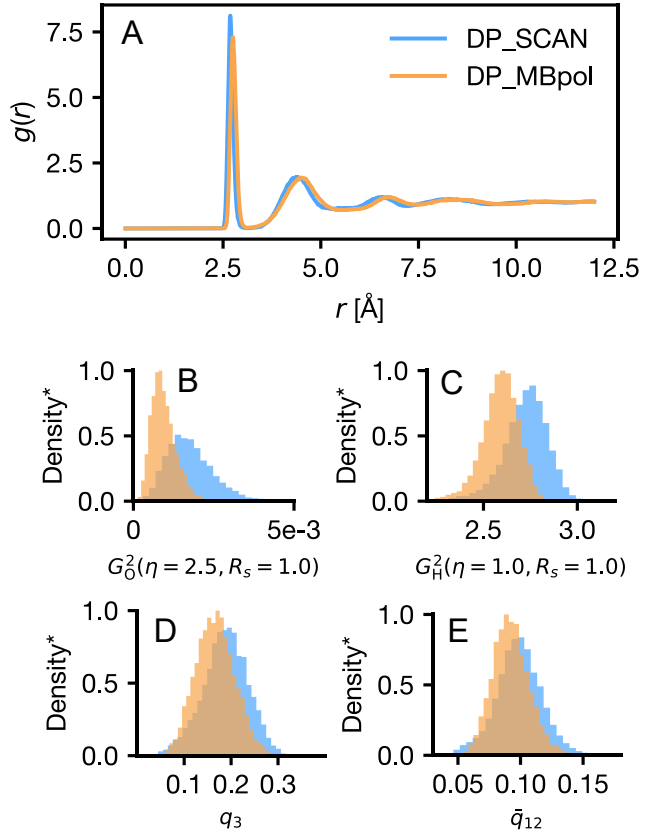


FIG. 9: Differences between local environments of generated LDA from DP_SCAN- and DP_MBpol. (A) Oxygen–oxygen radial distribution functions for LDA. (B–E) Distributions of select ACSF and BOO descriptors for LDA generated by each model. All probability densities are normalized such that the maximum value of either distribution is 1.0 (denoted as Density*). The blue and orange colors represent the DP_SCAN- and DP_MBpol models, respectively.

distinguish between amorphous phases. In this context, successful classification would imply systematic differences in local structure arising from the distinct potential energy surfaces encoded by each model.

We find that there are significant structural differences between LDA configurations produced by DP_SCAN versus DP_MBpol. We consider structural differences between HDA configurations in the SI, Fig S4. A classifier trained to distinguish LDA configurations from the two sources yields an accuracy rate of $77.5 \pm 0.3\%$ correct labels for unseen environments. This performance indicates that the two force fields produce measurably different local structures even within the same amorphous phase. The most informative features for making this distinction are exclusively atom-centered symmetry functions; no bond-orientational order parameters are retained (Table II). This suggests that DP_SCAN and DP_MBpol differ primarily in radial packing rather than orientational symmetry.

To better appreciate the physical differences between

the models, we contrast a series of conventional and local structural measures. The oxygen–oxygen radial distribution functions show a slightly higher short-range peak for DP_SCAN relative to DP_MBpol (Figure 9A), indicating a more compact local network in the DP_SCAN LDA phase. This is consistent with the higher LDA density predicted by DP_SCAN. The same behavior is captured more locally by the selected ACSF descriptors (Figures 9B,C). For both oxygen and hydrogen, DP_SCAN environments exhibit systematically higher local densities, *i.e.*, more neighbors at a given distance—than their DP_MBpol counterparts. These findings align with previous observations that SCAN-based water potentials tend to over-stabilize close-contact configurations [27, 44]. Orientational descriptors reveal more subtle differences. The distributions of q_3 and \bar{q}_{12} indicate that DP_MBpol produces slightly lower tetrahedral order and greater variability in local orientational environments (Figure 9D,E). Thus, while both models capture the overall tetrahedral topology of LDA, DP_MBpol generates a more distorted hydrogen-bond network.

IV. CONCLUSIONS

The microscopic character of the transformation between low-density and high-density amorphous ice has remained difficult to establish despite extensive experimental and computational study. By analyzing local atomic environments along pressure-induced compression and decompression pathways, we show that this transformation proceeds entirely through a redistribution between LDA-like and HDA-like local environments, with no evidence for intermediate structural states. The absence of additional populations provides compelling microscopic evidence consistent with first-order character, even in regimes where macroscopic thermodynamic observables vary smoothly.

Distinct microscopic pathways during compression and decompression reveal pronounced asymmetry in how tetrahedral networks collapse under pressure and subsequently reform, providing a molecular-level description of hysteresis in amorphous ice. The structural distinction between LDA and HDA is captured by a small set of physically interpretable local descriptors,

with hydrogen local density emerging as a particularly informative signature. These results clarify the microscopic basis of glass–glass interconversion in water and resolve ambiguities inherent to analyses based solely on bulk observables or single order parameters.

These conclusions are enabled by a probabilistic, interpretable framework for classifying local atomic environments that is explicitly capable of identifying out-of-distribution structures. This capability makes the absence of intermediate states a meaningful physical result rather than an artifact of the analysis. More broadly, the approach provides a general tool for probing local structure in disordered materials, comparing molecular models at the environment level, and diagnosing subtle structural differences that are not apparent from conventional metrics. The generality of this framework makes it broadly applicable to classification problems in computational materials science. In particular, as data-driven interatomic potentials become increasingly prevalent, such environment-resolved analyses will be essential for connecting microscopic structure to emergent condensed-phase behavior.

ACKNOWLEDGMENTS

Q.M.G. acknowledges support from the National Science Foundation Graduate Research Fellowship Program under Grant No. DGE-2039656. R.J.S., P.G.D., and M.A.W. acknowledge support from the “Chemistry in Solution and at Interfaces” (CSI) Center funded by the U.S. Department of Energy through Award No. DE-SC0019394. N.G. is thankful to the NSF (grant number CHE-2223461), and to the NSF-CREST Center for Interface Design and Engineered Assembly of Low Dimensional systems (IDEALS; grant numbers HRD-1547380 and HRD-2112550). Simulations and analyses were performed using resources from Princeton Research Computing at Princeton University, which is a consortium led by the Princeton Institute for Computational Science and Engineering (PICSciE) and Office of Information Technology’s Research Computing. All code required to recreate the results above can be obtained at <https://github.com/webbtheosim/amorphous-ice>.

[1] L. D. Landau, E. M. Lifshitz, E. M. Lifshits, and L. Pitaevskii, *Statistical physics: theory of the condensed state*, Vol. 9 (Butterworth-Heinemann, 1980).

[2] P. G. Debenedetti and F. H. Stillinger, Supercooled liquids and the glass transition, *Nature* **410**, 259 (2001).

[3] C. A. Angell, Amorphous water, *Annu. Rev. Phys. Chem.* **55**, 559 (2004).

[4] L. Berthier and G. Biroli, Theoretical perspective on the glass transition and amorphous materials, *Rev. Mod. Phys.* **83**, 587 (2011).

[5] S. Torquato and F. H. Stillinger, Local density fluctuations, hyperuniformity, and order metrics, *Phys. Rev. E* **68**, 041113 (2003).

[6] O. Mishima, L. Calvert, and E. Whalley, ‘melting ice’ at 77 K and 10 kbar: a new method of making amorphous solids, *Nature* **310**, 393 (1984).

[7] O. Mishima, L. Calvert, and E. Whalley, An apparently first-order transition between two amorphous phases of ice induced by pressure, *Nature* **314**, 76 (1985).

[8] P. H. Poole, F. Sciortino, U. Essmann, and H. E. Stanley, Phase behaviour of metastable water, *Nature* **360**, 324 (1992).

[9] P. Gallo, K. Amann-Winkel, C. A. Angell, M. A. Anisimov, F. Caupin, C. Chakravarty, E. Lascaris, T. Loerting, A. Z. Panagiotopoulos, J. Russo, *et al.*, Water: A tale of two liquids, *Chem. Rev.* **116**, 7463 (2016).

[10] H. Tanaka, Liquid–liquid transition and polyamorphism, *The Journal of Chemical Physics* **153**, 130901 (2020).

[11] P. G. Debenedetti, F. Sciortino, and G. H. Zerze, Second critical point in two realistic models of water, *Science* **369**, 289 (2020).

[12] N. Giovambattista, H. E. Stanley, and F. Sciortino, Potential-energy landscape study of the amorphous-amorphous transformation in h_2o , *Physical review letters* **91**, 115504 (2003).

[13] N. Giovambattista, F. Sciortino, F. W. Starr, and P. H. Poole, Potential energy landscape of the apparent first-order phase transition between low-density and high-density amorphous ice, *J. Chem. Phys.* **145**, 224501 (2016).

[14] J. Finney, A. Hallbrucker, I. Kohl, A. Soper, and D. Bowron, Structures of high and low density amorphous ice by neutron diffraction, *Phys. Rev. Lett.* **88**, 225503 (2002).

[15] T. Loerting, W. Schustereder, K. Winkel, C. G. Salzmann, I. Kohl, and E. Mayer, Amorphous ice: Stepwise formation of very-high-density amorphous ice from low-density amorphous ice at 125 K, *Phys. Rev. Lett.* **96**, 025702 (2006).

[16] P.-L. Chau and A. Hardwick, A new order parameter for tetrahedral configurations, *Molecular Physics* **93**, 511 (1998).

[17] J. R. Errington and P. G. Debenedetti, Relationship between structural order and the anomalies of liquid water, *Nature* **409**, 318 (2001).

[18] B. S. Jubes, M. Agarwal, and C. Chakravarty, Tetrahedral order, pair correlation entropy, and waterlike liquid state anomalies: Comparison of geo_2 with bef_2 , si_2 , and h_2o , *J. Chem. Phys.* **132**, 234507 (2010).

[19] P. J. Steinhardt, D. R. Nelson, and M. Ronchetti, Bond-orientational order in liquids and glasses, *Physical Review B* **28**, 784 (1983).

[20] F. Martelli, F. Leoni, F. Sciortino, and J. Russo, Connection between liquid and non-crystalline solid phases in water, *The Journal of Chemical Physics* **153**, 104503 (2020).

[21] Z. Faure Beaulieu, V. L. Deringer, and F. Martelli, High-dimensional order parameters and neural network classifiers applied to amorphous ices, *The Journal of Chemical Physics* **160**, 081101 (2024).

[22] R. Foffi and F. Sciortino, Correlated fluctuations of structural indicators close to the liquid–liquid transition in supercooled water, *J. Phys. Chem. B* **127**, 378 (2022).

[23] E. D. Donkor, A. Offei-Danso, A. Rodriguez, F. Sciortino, and A. Hassanali, Beyond local structures in critical supercooled water through unsupervised learning, *The Journal of Physical Chemistry Letters* **15**, 3996 (2024).

[24] S. Klotz, T. Strässle, R. Nelmes, J. Loveday, G. Hamel, G. Rousse, B. Canny, . f. J. Chervin, and A. Saitta, Nature of the polyamorphic transition in ice under pressure, *Phys. Rev. Lett.* **94**, 025506 (2005).

[25] J. Chiu, F. W. Starr, and N. Giovambattista, Pressure-induced transformations in computer simulations of glassy water, *J. Chem. Phys.* **139**, 184504 (2013).

[26] J. Wong, D. A. Jahn, and N. Giovambattista, Pressure-induced transformations in glassy water: A computer simulation study using the TIP4P/2005 model, *J. Chem. Phys.* **143**, 074501 (2015).

[27] R. J. Szukalo, N. Giovambattista, and P. G. Debenedetti, Computational investigation of water glasses using machine-learning potentials, *Proc. Natl. Acad. Sci. U.S.A.* **122**, e2509609122 (2025).

[28] D. Dhabal and V. Molinero, Kinetics and mechanisms of pressure-induced ice amorphization and polyamorphic transitions in a machine-learned coarse-grained water model, *J. Phys. Chem. B* **127**, 2847 (2023).

[29] G. Ramesh, V. Mahajan, D. Koner, and R. S. Singh, Microscopic pathways of transition from low-density to high-density amorphous phase of water, *The Journal of Chemical Physics* **160**, 194501 (2024).

[30] O. Mishima, Relationship between melting and amorphization of ice, *Nature* **384**, 546 (1996).

[31] T. Loerting, C. Salzmann, I. Kohl, E. Mayer, and A. Hallbrucker, A second distinct structural “state” of high-density amorphous ice at 77 K and 1 bar, *Physical Chemistry Chemical Physics* **3**, 5355 (2001).

[32] D. Perez, A. P. Subramanyam, I. Malivov, and T. D. Swinburne, Uncertainty quantification for misspecified machine learned interatomic potentials, *npj Computational Materials* **11**, 263 (2025).

[33] J. Behler, Atom-centered symmetry functions for constructing high-dimensional neural network potentials, *J. Chem. Phys.* **134**, 074106 (2011).

[34] A. P. Bartók, R. Kondor, and G. Csányi, On representing chemical environments, *Physical Review B—Condensed Matter and Materials Physics* **87**, 184115 (2013).

[35] R. S. DeFever, C. Targonski, S. W. Hall, M. C. Smith, and S. Sarupria, A generalized deep learning approach for local structure identification in molecular simulations, *Chemical science* **10**, 7503 (2019).

[36] J. Schmidt, M. R. Marques, S. Botti, and M. A. Marques, Recent advances and applications of machine learning in solid-state materials science, *npj computational materials* **5**, 83 (2019).

[37] M. Ceriotti, Unsupervised machine learning in atomistic simulations, between predictions and understanding, *The Journal of chemical physics* **150**, 150901 (2019).

[38] F. Musil, A. Grisafi, A. P. Bartók, C. Ortner, G. Csányi, and M. Ceriotti, Physics-inspired structural representations for molecules and materials, *Chemical Reviews* **121**, 9759 (2021).

[39] E. Boattini, M. Dijkstra, and L. Filion, Unsupervised learning for local structure detection in colloidal systems, *The Journal of chemical physics* **151**, 154901 (2019).

[40] C. Cai and T. Wang, Resolving chemical-motif similarity with enhanced atomic structure representations for accurately predicting descriptors at metallic interfaces, *Nature Communications* **16**, 8761 (2025).

[41] W. Lechner and C. Dellago, Accurate determination of crystal structures based on averaged local bond order parameters, *The Journal of chemical physics* **129**, 114707 (2008).

- [42] C. E. Shannon, A mathematical theory of communication, *The Bell System Technical Journal* **27**, 379 (1948).
- [43] J. Sun, A. Ruzsinszky, and J. P. Perdew, Strongly constrained and appropriately normed semilocal density functional, *Phys. Rev. Lett.* **115**, 036402 (2015).
- [44] L. Zhang, H. Wang, R. Car, and W. E, Phase diagram of a deep potential water model, *Phys. Rev. Lett.* **126**, 236001 (2021).
- [45] V. Babin, C. Leforestier, and F. Paesani, Development of a “first principles” water potential with flexible monomers: Dimer potential energy surface, VRT spectrum, and second virial coefficient, *J. Chem. Theory Comput.* **9**, 5395 (2013).
- [46] V. Babin, G. R. Medders, and F. Paesani, Development of a “first principles” water potential with flexible monomers. ii: Trimer potential energy surface, third virial coefficient, and small clusters, *J. Chem. Theory Comput.* **10**, 1599 (2014).
- [47] G. R. Medders, V. Babin, and F. Paesani, Development of a “first-principles” water potential with flexible monomers. iii. liquid phase properties, *J. Chem. Theory Comput.* **10**, 2906 (2014).
- [48] S. L. Bore and F. Paesani, Realistic phase diagram of water from “first principles” data-driven quantum simulations, *Nat. Comm.* **14**, 3349 (2023).
- [49] A. P. Thompson, H. M. Aktulga, R. Berger, D. S. Bolintineanu, W. M. Brown, P. S. Crozier, P. J. In’t Veld, A. Kohlmeyer, S. G. Moore, T. D. Nguyen, *et al.*, LAMMPS-a flexible simulation tool for particle-based materials modeling at the atomic, meso, and continuum scales, *Comput. Phys. Commun.* **271**, 108171 (2022).
- [50] L. Zhang, J. Han, H. Wang, R. Car, and W. E, Deep potential molecular dynamics: a scalable model with the accuracy of quantum mechanics, *Phys. Rev. Lett.* **120**, 143001 (2018).
- [51] H. Wang, L. Zhang, J. Han, and E. Weinan, DeePMD-kit: A deep learning package for many-body potential energy representation and molecular dynamics, *Comput. Phys. Commun.* **228**, 178 (2018).

Supporting Information for “A Local Structural Basis to Resolve Amorphous Ices”

Quinn M. Gallagher^{1,†}, Ryan J. Szukalo^{2,†}, Nicolas Giovambattista^{3,4}, Pablo G. Debenedetti¹, Michael A. Webb^{1,*}

¹Department of Chemical and Biological Engineering, Princeton University, Princeton, NJ 08544, United States

²Department of Chemistry, Princeton University, Princeton, NJ 08544, United States

³Department of Physics, Brooklyn College of the City University of New York, Brooklyn, New York 11210, United States

⁴Ph.D. Programs in Physics and Chemistry, The Graduate Center of the City University of New York, New York, NY 10016, United States

[†]These authors contributed equally to this work.

*Corresponding Author: mawebb@princeton.edu

Contents

S1. Benchmarking Model Performance for DP_SCAN Environments	2
S2. Out-of-distribution Predictions for DP_SCAN and DP_MBpol Environments	3
S3. Sensitivity of Structural Pathways to Selected Feature Spaces	4
S4. Differences between DP_SCAN- and DP_MBpol-generated HDA Environments	6

Appendix S1: Benchmarking Model Performance for DP_SCAN Environments

In the main text, Section III.A. reports the precisions, recalls, and accuracies of BOO-NN, PointNet, AE-GMM, and the present work on LDA/HDA classification for local atomic environments generated by DP_MBpol. We report the same results for local atomic environments generated by DP_SCAN in Table I.

TABLE S1: Comparison of model performance for classification of DP_SCAN-generated LDA/HDA environments. Values represent the mean and standard deviation over five-fold cross-validation.

Model	HDA-Precision	HDA-Recall	LDA-Precision	LDA-Recall	Accuracy
BOO-NN	0.947 ± 0.007	0.997 ± 0.001	0.997 ± 0.001	0.945 ± 0.007	0.971 ± 0.003
PointNet	0.937 ± 0.008	0.988 ± 0.003	0.988 ± 0.003	0.934 ± 0.008	0.961 ± 0.003
AE-GMM	0.938 ± 0.008	0.982 ± 0.003	0.983 ± 0.003	0.935 ± 0.008	0.959 ± 0.003
Present Work (BOO)	0.951 ± 0.006	0.977 ± 0.008	0.978 ± 0.008	0.950 ± 0.005	0.964 ± 0.006
Present Work (ACSF)	0.935 ± 0.010	0.997 ± 0.001	0.998 ± 0.001	0.931 ± 0.010	0.964 ± 0.005
Present Work (BOO+ACSF)	0.948 ± 0.006	0.987 ± 0.004	0.988 ± 0.004	0.945 ± 0.005	0.967 ± 0.004

Performance metrics are lower for classifying environments generated by DP_SCAN than they are for DP_MBpol. Table I in the main text shows that accuracies for some models are greater than 0.99 for DP_MBpol environments, while here all accuracies are roughly between 0.96-0.97 for DP_SCAN environments. The relative performance of the models, however, is similar; BOO-NN and our work perform best, followed by PointNet and AE-GMM. These results agree with what is observed for DP_MBpol environments: our work maintains comparable accuracy to deep learning methods while adopting a physically interpretable classification scheme. Interestingly, BOO-NN, AE-GMM, and our work show higher HDA recall and LDA precision than HDA precision and LDA recall. This indicates that these models are liberal in their assignment of HDA but conservative in their assignment of LDA, suggesting a relationship between HDA and LDA structures for DP_SCAN not present in DP_MBpol.

Appendix S2: Out-of-distribution Predictions for DP_SCAN and DP_MBpol Environments

In the main text, Section III.A. analyzes the behavior of BOO-NN, PointNet, AE-GMM, and the present work when making predictions on out-of-distribution atomic environments. Specifically, models are trained on HDA and LDA atomic environments, but are used to predict the labels of hexagonal ice (Ih) atomic environments. In the main text, we only perform this analysis for environments generated by DP_MBpol. Here, we report the same results for DP_SCAN configurations.

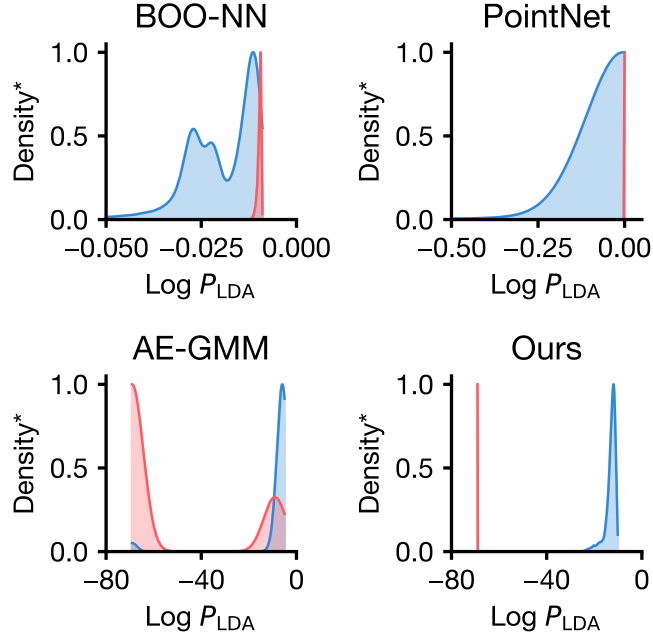


FIG. S1: Predicted LDA log probabilities from (A) BOO-NN, (B) PointNet, (C) AE-GMM, and (D) our work applied to DP_SCAN-generated environments of LDA and hexagonal ice (Ih). Distributions for true LDA configurations are shown in blue, while distributions for Ih configurations are shown in red. Each density is normalized so that its maximum value is 1.0.

As observed in the main text, BOO-NN (Fig. S1A) and PointNet (Fig. S1B) struggle to separate LDA and Ih distributions, and these models confidently label Ih environments as LDA. Accordingly, the present work is capable of accurately distinguishing Ih environments as outliers from those on which the model was trained (*i.e.*, LDA and HDA), as shown by the separation between the distributions in Figure S1D. Interestingly, while AE-GMM (Fig. S1C) was capable of detecting outliers for DP_MBpol environments, this model struggles to do so for configurations generated by DP_SCAN. Such a result demonstrates the utility of considering all available features, as is done in our work, relative to density estimation on reduced feature spaces, as is done by AE-GMM.

Appendix S3: Sensitivity of Structural Pathways to Selected Feature Spaces

In the main text, Section III.F analyzes how the evolution of average atomic environments proceeds during compressions and decompressions across a range of temperatures. We show these evolutions for DP_MBpol and DP_SCAN for two different feature spaces. Here, we show these evolutions for 25 feature spaces comprised of each pair of features selected by our model to be most informative for accurate LDA/HDA classification.

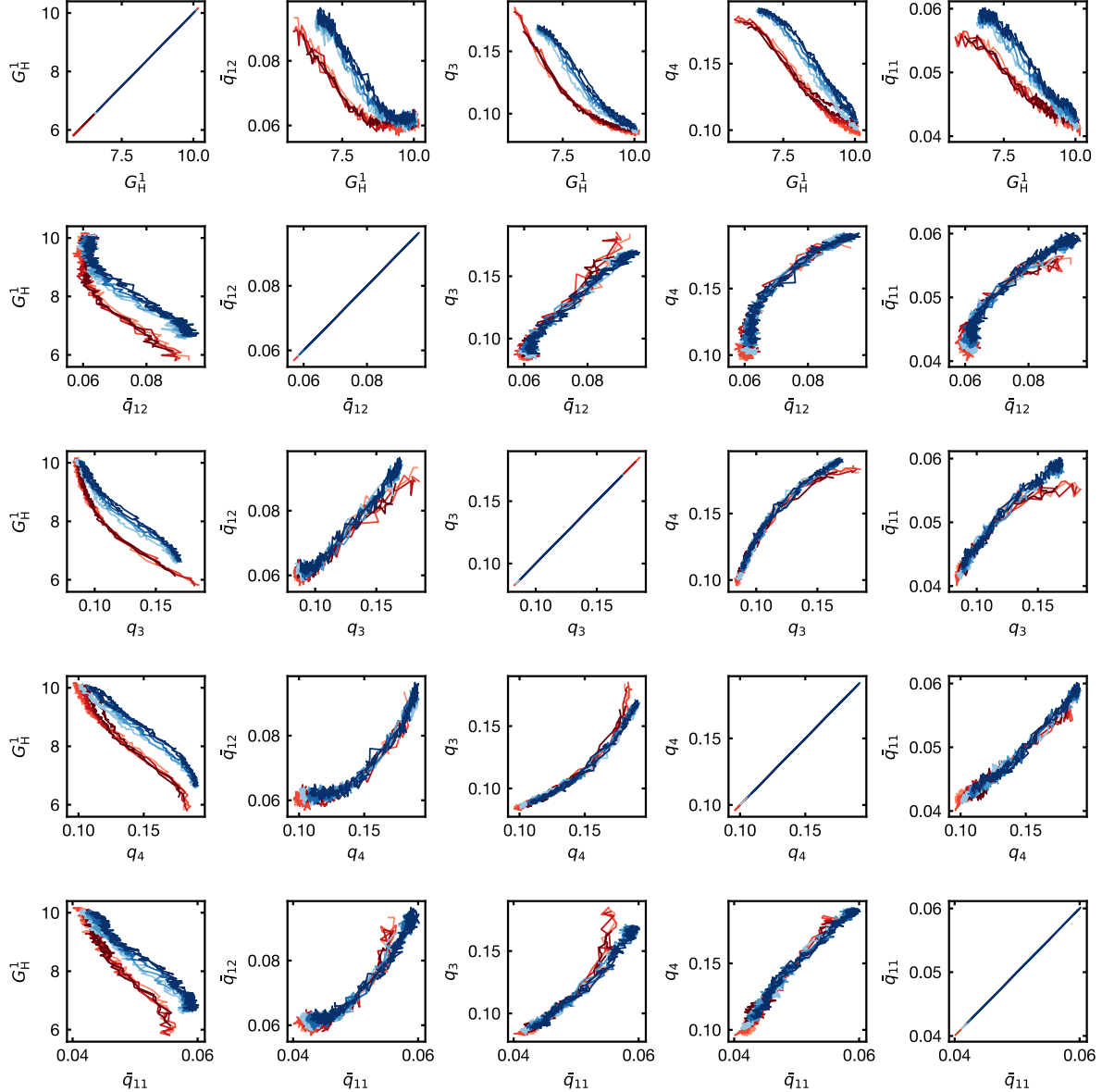


FIG. S2: Evolution of average local environment descriptors during compressions (blue) and decompressions (red) at temperatures from 60 K to 140 K for the DP_MBpol force field. Descriptors are plotted in feature spaces for every pair of features selected by our model for LDA/HDA classification.

Results from Figures S2 and S3 corroborate the results discussed in Section III.F. Namely, we observe a hysteresis in environment pathways when considering feature spaces that consist of an ACSF and BOO, but this separation is not visible when visualizing pairs of BOOs. Therefore, it is necessary to consider both radial and spherical information to identify differences in the structural pathways taken by compressions and decompressions—an observation that would go unnoticed if we relied solely on the BOOs employed in previous studies.

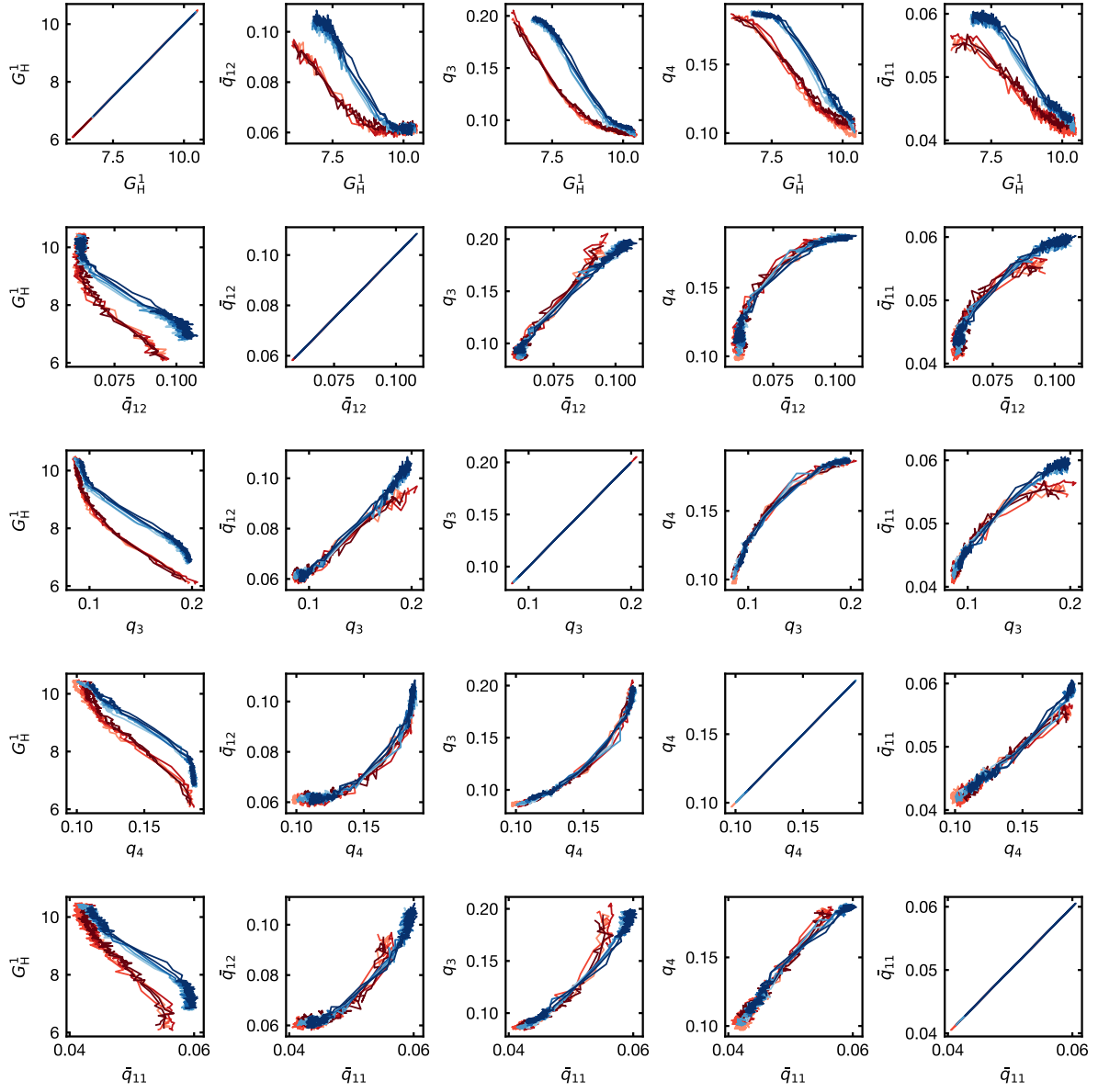


FIG. S3: Evolution of average local environment descriptors during compressions (blue) and decompressions (red) at temperatures from 60 K to 140 K for the DP_SCAN force field. Descriptors are plotted in feature spaces for every pair of features selected by our model for LDA/HDA classification.

Appendix S4: Differences between DP_SCAN- and DP_MBpol-generated HDA Environments

In the main text, Section III.G analyzes structural differences between LDA environments generated by DP_SCAN and DP_MBpol. Here, we consider structural differences between HDA environments generated by the same two force fields. Our classifier can distinguish between DP_SCAN and DP_MBpol HDA environments with an accuracy of $64.3 \pm 0.03\%$, indicating that there are structural differences (albeit less than LDA) present in these environments. We consider how distributions of DP_SCAN and DP_MBpol environments vary along a select set of structural descriptors with high mutual information for DP_SCAN/DP_MBpol classification, which we visualize in Figure S4.

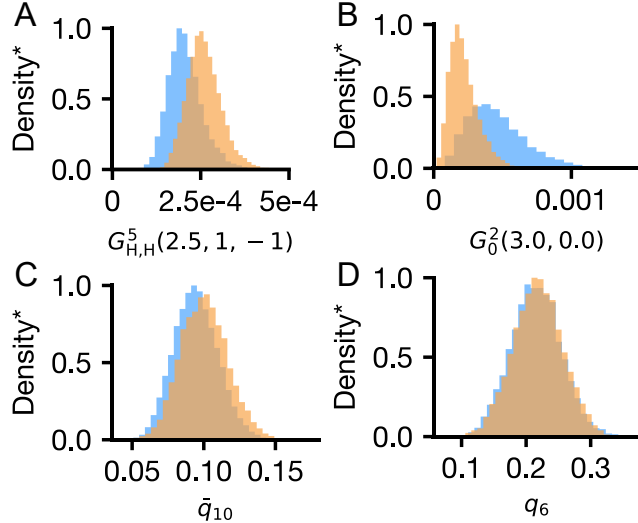


FIG. S4: Differences between local environments of HDA generated from DP_SCAN and DP_MBpol. (A–D) Distributions of select ACSF and BOO descriptors for HDA generated by each model. All probability densities are normalized such that the maximum value of either distribution is 1.0 (denoted as Density*). The blue and orange colors represent the DP_SCAN and DP_MBpol models, respectively.

Figures S4A and S4B show distributions of DP_SCAN and DP_MBpol environments along the two most informative features identified by our classifier. One can clearly observe differences in the two distributions, suggesting that (similar to LDA environments) DP_SCAN and DP_MBpol disagree most in their reproduction of interatomic distances. This is most directly observed when considering the second descriptor, $G_O^2(3.0, 0, 0)$, where higher values indicate reduced oxygen–oxygen pairwise distances. Figures S4C and S4D show distributions of DP_SCAN and DP_MBpol environments along the two most informative BOOs. HDA environments appear to have similar distributions along these descriptors, indicating that DP_SCAN and DP_MBpol predict similar spherical symmetry in HDA environments.